Title

Benzyl Alcohol Photo-oxidation Based on Molecular Electronic Transitions in Metal Halide Perovskites

Journal

ACS Photonics, 10(3)

ISSN

2330-4022

Authors

Jin, Jianbo
Huang, Haowei
Chen, Chubai
et al.

Publication Date

2023-03-15

DOI

10.1021/acsphotonics.3c00042

Peer reviewed

Benzyl Alcohol Photo-oxidation based on Molecular Electronic Transitions in Metal Halide Perovskites

Jianbo Jin[1,2,#], Haowei Huang[1,8,#], Chubai Chen[1], Patrick W. Smith[4], Maria C. Folgueras[3,7], Sunmoon Yu[3], Ye Zhang[1], Peng-Cheng Chen[1,7], Fabian Seeler[6], Bernd Schaefer[6], Carlos Lizandara-Pueyo[2], Rui Zhang[2], Kerstin Schierle-Arndt[2,6], and Peidong Yang[*,1,2,3,4,5,7]

1 Department of Chemistry, University of California, Berkeley, California 94720, United States

2 California Research Alliance (CARA), BASF Corporation, Berkeley, California 94720, United States

3 Department of Materials Science and Engineering, University of California, Berkeley, California 94720, United States

4 Chemical Sciences Division, Lawrence Berkeley National Laboratory, Berkeley, California 94720, United States

5 Materials Sciences Division, Lawrence Berkeley National Laboratory, Berkeley, California 94720, United States

6 BASF SE, 67056 Ludwigshafen am Rhein, Germany

7 Kavli Energy NanoScience Institute, Berkeley, California 94720, United States

8 cMACS, Department of Microbial and Molecular Systems, KU Leuven, Celestijnenlaan 200F, 3001 Leuven, Belgium

[#] J.J. and H.H. contributed equally

* Email: p_yang@berkeley.edu

ABSTRACT:

Vacancy ordered double perovskites $Cs_2Te(IV)X_6$ have been found to exhibit molecule-like electronic behavior when X is Cl^- or Br^- due to the zero-dimensional (0D) nature of their octahedral units. Electronically isolated building block, the $[TeBr_6]^{2-}$ ionic octahedron, serves as the fundamental electronic unit of the Cs_2TeBr_6 solid. Herein, a detailed understanding of the Cs_2TeBr_6 electronic structure and its photoexcitation is presented with the consideration of individual molecular orbitals from these isolated octahedral building blocks. Two optical absorption features correspond to two unique electronic transitions, (1) a highest occupied molecular orbital (HOMO) to lowest unoccupied molecular orbital (LUMO) transition under 455 nm excitation and (2) mixed transitions including lower HOMO states to LUMO transition, and HOMO to higher LUMO states transition under 365 nm excitation. With this in mind, we examined the excitation wavelength dependent photo-oxidation of benzyl alcohol using Cs_2TeBr_6 as photocatalysts. Significant differences in photocatalytic performance are observed and different forms of activated alcohol radicals are detected under the two excitation wavelengths. As a case study, this work highlights the application of molecule-like halide perovskites in photocatalysis. The highly tunable energy band structures and catalytic centers in perovskites can offer a valuable platform for photocatalytic mechanistic studies and catalyst development in the foreseeable future.

KEYWORDS: *Halide Perovskites, Photocatalysis, Molecular, Electronic Transition, Organic Transformation*

INTRODUCTION

Metal halide perovskites are a family of emergent semiconductors with remarkable optoelectronic properties[1,2] and rich structural chemistry.[3] Halide perovskite materials have been widely applied in photovoltaics,[4–7] light-emitting diodes,[8,9] photodetectors,[10,11] and other fields due to their tunable band gaps, facile synthesis, high absorption coefficients, and high charge mobilities.[12,13] Recently, semiconductor materials have been more extensively applied to drive photocatalytic reactions including water splitting,[14–16] small molecule activation,[17,18] and organic transformation.[19–23] Material systems based on pure metal halide perovskites, or composite materials of perovskites and other semiconductors or metals, have been shown as new platforms for carrying out photocatalysis.[24,25]

Vacancy ordered double perovskites, with the formula of $Cs_2M(IV)X_6$, are formed when every two adjacent B^{2+} sites of the traditional ABX_3 perovskite structure are occupied by a M^{4+} cation (e.g., Te^{4+}, Sn^{4+}, Pt^{4+}, Ti^{4+}) and a vacancy.[26,27] The $[M(IV)X_6]^{2-}$ octahedra are stacked in the face-centered cubic (FCC)-type lattice in the $Cs_2M(IV)X_6$ halide perovskites. As a result, the $[M(IV)X_6]^{2-}$ octahedra are more electronically isolated due to the zero-dimensional (0D) nature of this halide perovskite structure. Our previous work on Cs_2TeX_6 has revealed that this electronic isolation of the $[TeX_6]^{2-}$ ionic octahedra leads to a change in the electronic bands of Cs_2TeX_6 from discrete forms in the Cl^- to Br^- versions to continuous ones in the I^- version, indicating that the Cs_2TeCl_6 and Cs_2TeBr_6 systems are more molecule-like in comparison to Cs_2TeI_6. This is further confirmed by the molecule-like absorption features in the Cs_2TeCl_6 and Cs_2TeBr_6 systems.[28,29] Compared with the three-dimensional (3D) or two-dimensional (2D) counterparts,[19,22,23,30] the 0D molecule-like halide perovskites can have multiple electronic

transitions, with the formation of energy specific photo-generated holes, to enable various catalytic reactions. Currently, most photocatalytic works are based on the 3D or 2D halide perovskites, with very little attention being devoted to these 0D systems, let alone their molecule-like properties.

RESULTS

Ligand-free Cs_2TeBr_6 (CTB) powders in the size range of hundreds of nanometers (**Figure S1**) were synthesized through a facile solution synthesis as described in the Supporting Information. The composition of the nano and micro powders is confirmed by energy-dispersive X-ray spectroscopy (EDS, **Figure S2**) with a formula of Cs:Te:Br = 2:1.023:6.076. **Figure S3** shows the X-ray photoelectron spectroscopy (XPS) survey scans of CTB powders, which further prove the approximate 2-1-6 composition. The low signal intensity of C 1s also indicates that the powders are ligand-free. The powder X-ray diffraction (PXRD) pattern of CTB powders matches perfectly with the calculated patterns of the FCC unit cell, which reveals that CTB is an FCC solid assembly of $[TeBr_6]^{2-}$ ionic octahedra. (**Figure S4)**.

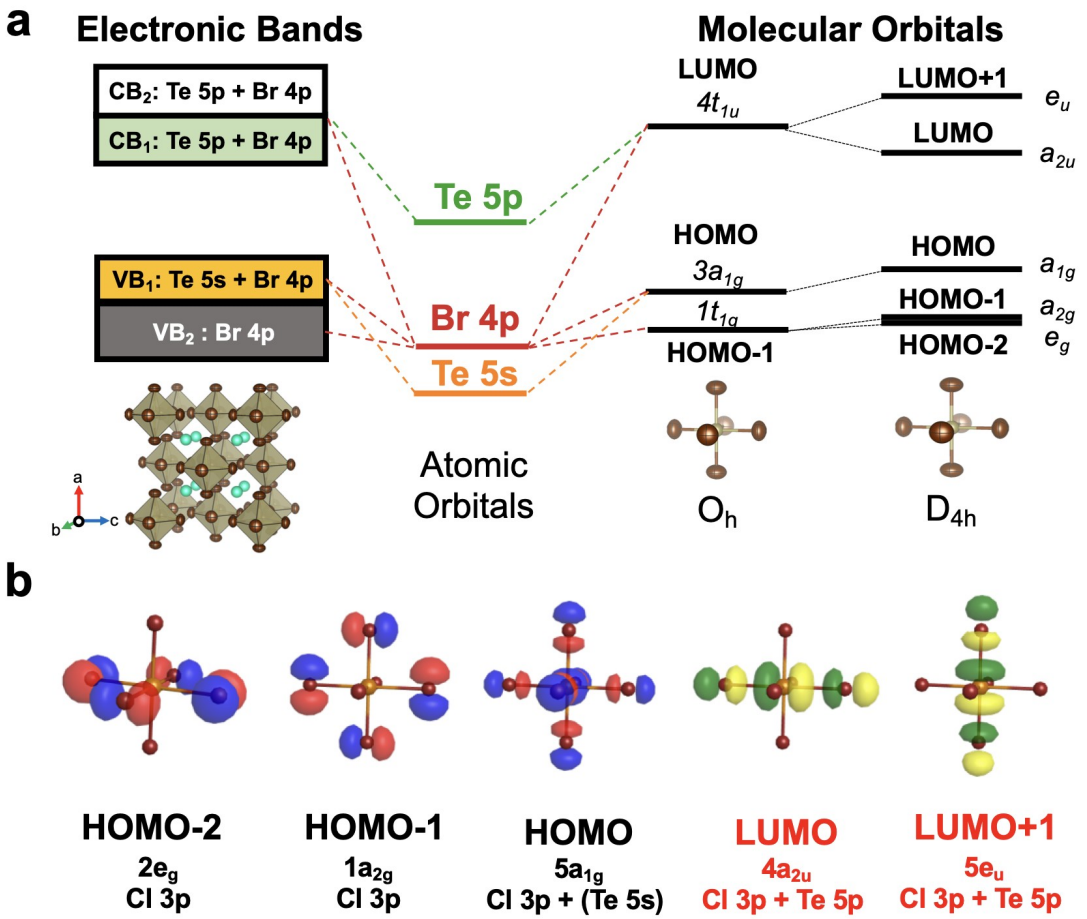

Figure 1. Electronic Band Structure of Cs_2TeBr_6 and Molecular Orbitals of An Individual $[TeBr_6]^{2-}$ Ionic Octahedron (a) Molecular orbital energy diagram of O_h and D_{4h} $[TeBr_6]^{2-}$ ionic octahedra, and a schematic of the electronic band structure of Cs_2TeBr_6. (b) Selected frontier molecular orbitals (MOs) of a D_{4h} $[TeBr_6]^{2-}$ ionic octahedron: the LUMO and LUMO+1 are the $4a_{2u}$ and $5e_u$ state, respectively, forming by Te 5p and Br 4p orbitals; the HOMO is the $5a_{1g}$ state contributed by Te 5s and Br 4p orbitals; the HOMO-1 and HOMO-2 are $1a_{2g}$ and $2e_g$ state, respectively, fully contributed by Br 4p orbitals.

Our previous studies reveal that the $[TeBr_6]^{2-}$ ionic octahedron is the electronic unit and vibrational unit of the CTB solids.[28] Therefore, the electronic transitions of an individual $[TeBr_6]^{2-}$ ionic octahedron are essential for a comprehensive understanding of the electronic transitions in CTB solids. **Figure 1a** illustrates the correlation between the electronic bands of CTB solids and the molecular orbitals (MOs) of the $[TeBr_6]^{2-}$ octahedron. For the $[TeBr_6]^{2-}$ ionic octahedron in the O_h point group, its electron configuration is

$1a_{1g}^2 1t_{1u}^6 1e_g^4 2a_{1g}^2 2t_{1u}^6 1t_{2g}^6 2e_g^4 3t_{1u}^6 1t_{2u}^6 1t_{1g}^6 3a_{1g}^2 4t_{1u}^0$.[31,32] The lowest unoccupied molecular orbital (LUMO) is the $4t_{1u}$ state constructed from the Te 5p and Br 4p orbitals, while the highest occupied molecular orbital (HOMO) is the $3a_{1g}$ state, which is a hybridization of the Te 5s and Br 4p orbitals. Importantly, the first MO below the HOMO (marked as "HOMO-1") is the $4t_{1g}$ state fully contributed by non-bonding Br 4p orbitals. The details of the MO calculations are shown in **Table S1**. The electronic band structure of CTB is in good agreement with the MO diagram of $[TeBr_6]^{2-}$. According to the partial density of states (PDOS) from the density function theory (DFT) calculation,[28] the frontier band structure can be classified into three electronic bands (**Figure S5**), which are a conduction band (CB) constructed from Te 5p and Br 4p orbitals, the highest valence band (VB_1) formed by the hybridized Te 5s and Br 4p orbitals, and the band directly below the highest VB (marked as "VB_2") constructed from Br 4p orbitals. It is worth noting that the triplet CB will split into a doublet CB (marked as "CB_2") and a singlet CB (marked as "CB_1") due to the spin-orbital coupling (SOC) effects. The band structure with SOC effects can still be described by the MO diagrams of a photoexcited $[TeBr_6]^{2-}$ octahedron in a D_{4h} point group due to a dynamic Jahn-Teller distortion.[33–35] For the $[TeBr_6]^{2-}$ ionic octahedron in the D_{4h} point group, the 3-fold symmetry is no longer existing, the details of the MO calculations are shown in **Table S2**. The triplet LUMO in the O_h point group ($4t_{1u}$) splits into a singlet a_{2u} state (LUMO), and a higher doublet e_u state (marked as "LUMO+1"), while the original triplet HOMO-1 ($1t_{1g}$ state) also splits into an a_{2g} state (marked as "HOMO-1") and an e_g state (marked as "HOMO-2"). **Figure 1b** shows the shapes and symmetry of the frontier MOs of the D_{4h} $[TeBr_6]^{2-}$. The LUMO and LUMO+1 orbitals are still constructed from the Te 5p and Br 4p orbitals, the HOMO is the a_{1g} state hybrid by the Te 5s and Br 4p orbitals, and the HOMO-1 and

HOMO-2 orbitals are fully contributed by non-bonding Br 4p orbitals. Based on the studies of the $[TeBr_6]^{2-}$ octahedron, we can understand the nature of each frontier band for the CTB solids.

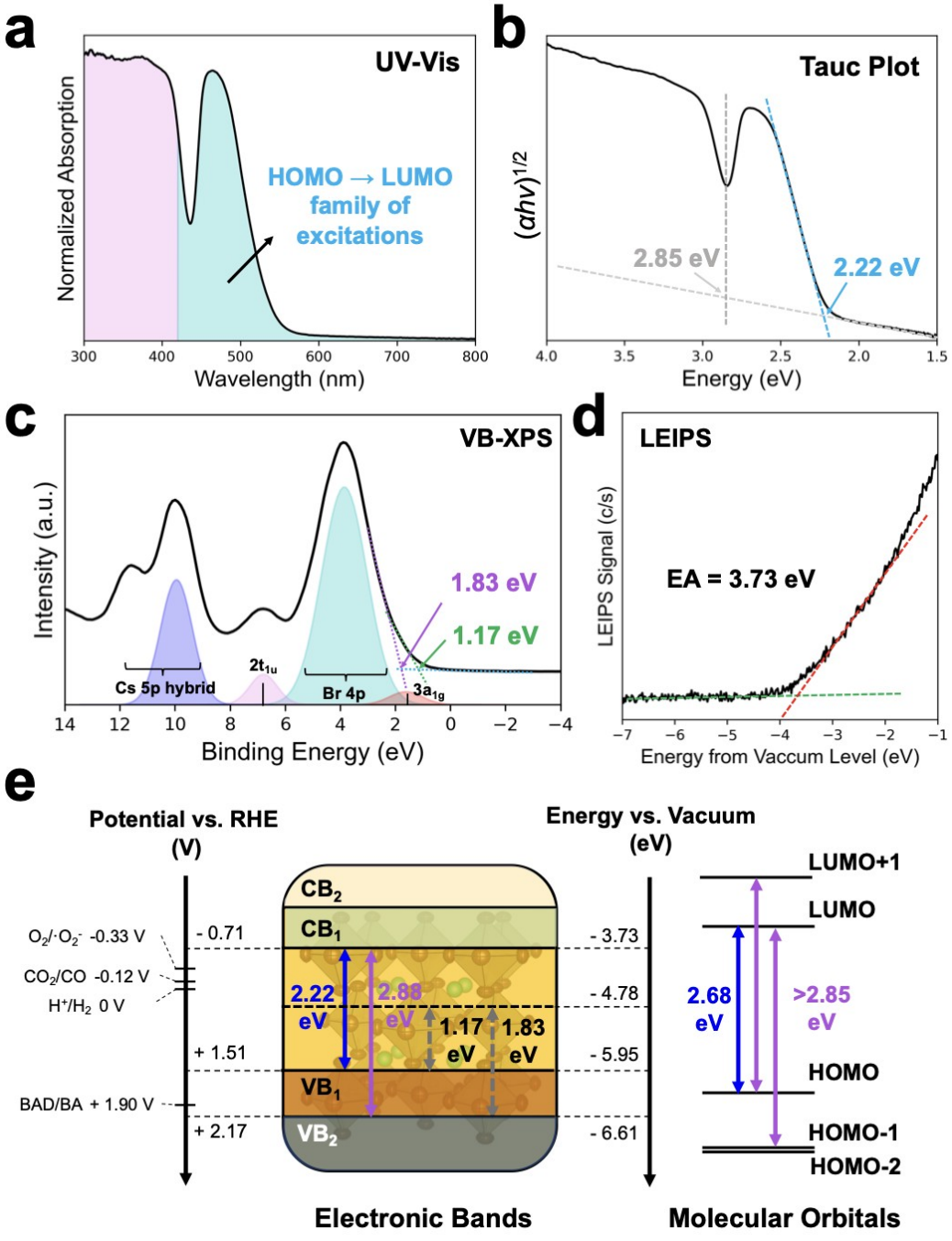

Figure 2. Photoexcitation and Electronic Band Structure of Cs_2TeBr_6. (a) UV-vis absorption spectrum of Cs_2TeBr_6 powders. (b) Tauc Plot for Cs_2TeBr_6 based on an indirect bandgap assignment. (c) VB-XPS of Cs_2TeBr_6. The two band edges of VB_1 and VB_2 are estimated to be

1.17 eV and 1.83 eV vs. its Fermi level, respectively. (d) LEIPS of Cs_2TeBr_6. The electron affinity (EA) is estimated as 3.73eV. (e) The comprehensive energy diagram of Cs_2TeBr_6 vs. the vacuum level and selected reaction redox potentials.

Optical and photoelectron spectroscopic characterizations are applied to quantitatively investigate the electronic band structure. A molecule-like absorption feature is observed in the UV-vis absorption spectra of the CTB powders (**Figure 2a**, highlighted in blue). Based on the frontier band structure identified above, the molecule-like absorption peak across 2.2-2.8 eV, akin to the "A band" in the $[TeBr_6]^{2-}$ absorption spectra, is attributed to the HOMO-to-LUMO transition.[31,33,34] **Figure 2b** shows the Tauc plot of CTB based on the indirect bandgap model. 2.22 eV is identified as the indirect bandgap value of CTB, while 2.68 eV is the maximum wavelength (λ_{max}) of this molecule-like absorption. Absorbance from the second group of transitions, akin to the "B band" in the $[TeBr_6]^{2-}$ absorption spectra, occurs when the excitation energy is higher than 2.85 eV. In a manner similar to electronic transitions in Au cluster systems,[36,37] a group of specific transitions from a deeper state, or specific transitions towards a higher state can be facilitated by photons of higher energy. As a result, the electronic transitions in this region could refer to three transitions, including HOMO-1-to-LUMO, HOMO-2-to-LUMO, and HOMO-to-LUMO+1.[31,34] Valence band X-ray photoelectron spectroscopy (VB-XPS) in **Figure 2c** shows the detailed VB structures of CTB. Each component of the VB has been identified based on a previous study.[31] The $3a_{1g}$ state occurs as a shoulder peak to the major Br 4p peak, which is clearer in the case of Cs_2TeCl_6 (**Figure S6**). This agrees with our observation that the electronic bands in CTB are more dispersive than Cs_2TeCl_6.[28] As a result, the band edges of the VB_1 band and the VB_2 band are estimated as 1.17 eV and 1.83 eV relative to its Fermi level, respectively. Low energy inverse photoemission spectroscopy (LEIPS) is performed to find the absolute value of the conduction band minimum (CBM), which is

determined as -3.73 eV vs. the vacuum level (E_{vac}) (**Figure 2d**). The corresponding low energy electron transmission (LEET) spectrum is in **Figure S7**. Flat-band measurement is applied to further confirm the CBM potential. And the Mott-Schottky plot of CTB suggests a CBM value of -0.97 V vs Ag/AgCl (3 M KCl) reference electrode (**Figure S8**), which is -3.68 eV vs E_{vac}., and it matches very well with the LEIPS result under vacuum. The combination of these results yields relative energy levels for this molecule-like CTB in **Figure 2e**. Detailed calculation processes for each energy level is shown in **Figure S9**. The CBM and VBM are -3.73 eV and -5.97 eV with respect to the vacuum level, respectively. The band edge of the VB_2 band is estimated as -6.63 eV vs. E_{vac}. The energy gap for the second group of transitions is then calculated to be 2.90 eV, perfectly in alignment with our observations in the UV-vis absorption spectrum. Compared to the potentials for several typical redox reactions, we find that the CBM of CTB is above $\varphi_{O_2/\cdot O_2^-}$ (-0.33 V vs. normal hydrogen electrode, NHE), while benzyl alcohol-to-benzaldehyde $\varphi_{BA/BAD}$ (+1.98 eV vs. NHE)[38] is in between the two VB energy levels. Thus, in order to realize the photocatalytic benzyl alcohol (BA) oxidation reactions, we could rationally photo-activate the CTB system with UV light to generate energy-sufficient holes at the deeper valence band (the VB_2 band).

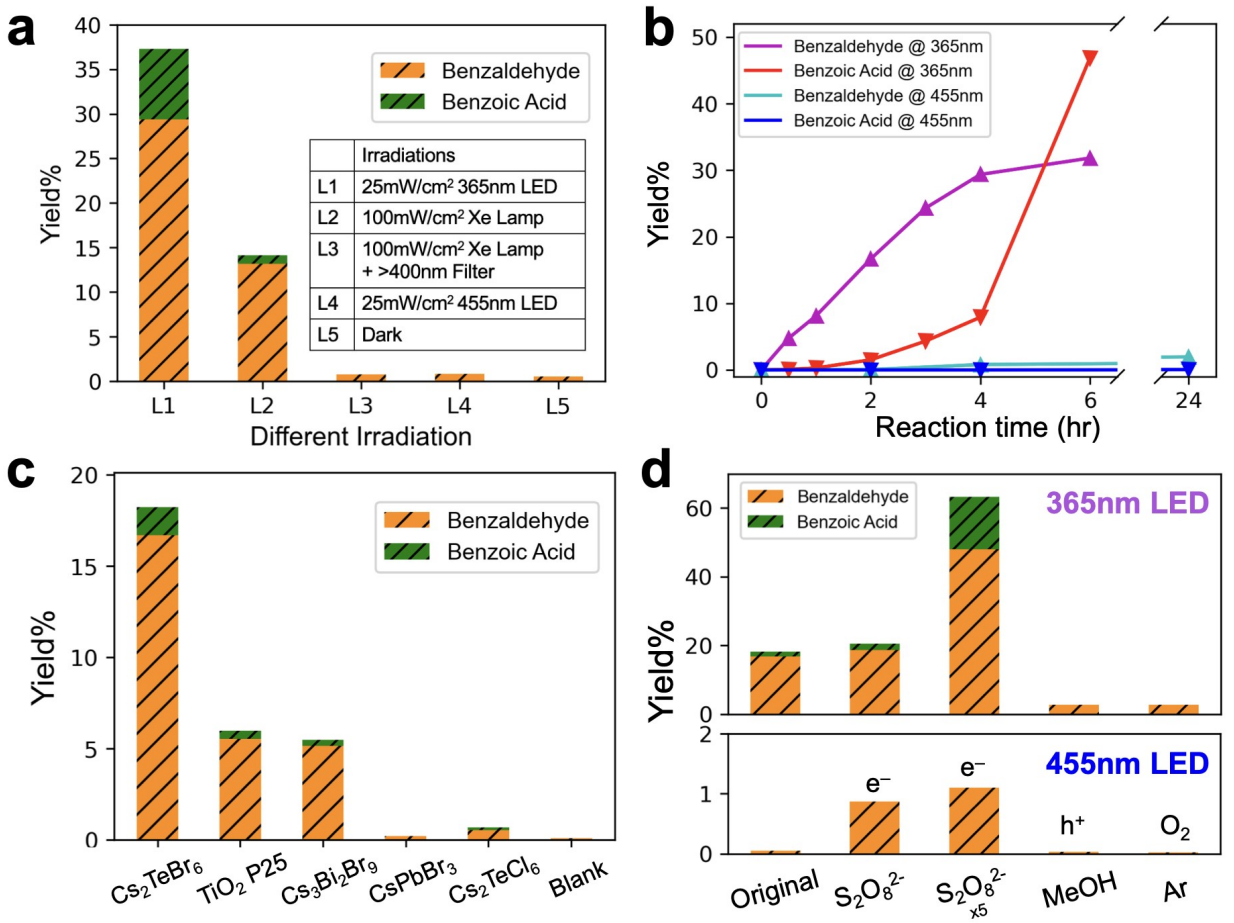

Figure 3. Photocatalytic Behavior of Cs_2TeBr_6. (a) Photocatalytic behavior of Cs_2TeBr_6 on benzyl alcohol oxidation under different light irradiation. (b) Photocatalytic performance of Cs_2TeBr_6 on benzyl alcohol oxidation. (c) Comparison of the photocatalytic performance of Cs_2TeBr_6 with other semiconductors. (d) Photocatalytic performance of Cs_2TeBr_6 on benzyl alcohol oxidation with different sacrificial agents under both 365 nm and 455 nm LED. All experiment details and conditions are listed in supporting information.

First, different excitation wavelengths are used to excite particular electronic transitions in CTB for photocatalytic BA oxidation, including a 365 nm UV LED, a 455 nm blue LED, and a Xe lamp with and without a 400nm long pass filter. The photocatalytic efficiencies are shown in **Figure 3a** and **Table S3**, which clearly demonstrate that the performance is fully dominated by UV photon excitation. The reaction is later carefully quantified under a 365 nm and a 455 nm LED (**Figure 3b**), and we find that the formation of benzaldehyde (BAD) linearly increases in the first 3 hours, with over-oxidation towards benzoic acid occurring after 2hr. CTB shows

efficient photocatalytic behavior of 16.69 μmol BAD and 1.52 μmol benzoic acid in 2 hr under 365 nm excitation, but it performs poorly with less than 2 μmol BAD in 24 hr under 455 nm excitation, even though the powders have strong absorption at 455 nm. And the performances of CTB under 365nm can be well maintained over 4 cycles. (**Figure S10** and **Table S4**) Compared to other semiconductor photocatalysts and halide perovskite materials, including commercial TiO_2 P25, $Cs_3Bi_2Br_9$, $CsPbBr_3$, and Cs_2TeCl_6, CTB exhibits superior photocatalytic performance for BA oxidation under 365 nm excitation (**Figure 3c** and **Table S5**). Due to molecular electronic transition nature for the 0D halide perovskites, the holes derived from relatively discreet and deeper energy states of CTB can be generated using 365 nm photons and be used for our oxidation reaction. In comparison, for 3D ($CsPbBr_3$) and 2D ($Cs_3Bi_2Br_9$) halide perovskites and semiconductors (TiO_2 P25) with more dispersed energy bands, holes generated from high energy UV photons tend to thermalize rapidly to the VBM level, which become less energetic towards the oxidation reaction. This difference in the excitation results in a higher photocatalytic performance for our CTB system.

Understanding the photocatalytic mechanism at the molecular level is crucial to explain the differences in performance under the two different excitation wavelengths. **Figure S11** represents the typical molecular pathways for alcohol oxidation on a semiconductor photocatalyst.[39–41] **Figure S11a** shows the superoxide radical-involved reaction mechanism. Under light excitation, an electron-hole pair will be generated, thermalized, and transported to the surface of the catalyst. The photogenerated electrons will be utilized to reduce the O_2 into a superoxide radical ($\cdot O_2^-$), while the holes will be used to activate the alcohol to produce alcohol radicals. The alcohol radicals will be oxidized into aldehyde after the radical reacts with

superoxide radicals. **Figure S11b** represents a direct oxidation mechanism, where the electron in the CB is not used to form superoxide radicals, and two holes are used to oxidize the alcohol into aldehyde. To probe the photocatalytic mechanism of the molecule-like CTB halide perovskites, various sacrificial agents are added to the reaction (**Table S6**). Sacrificial agents are selected based on their inertness to the photocatalytic reactions and to the photocatalysts themselves. Thus, methanol (MeOH) and ammonium persulfate ($2NH_4^+$ $S_2O_8^{2-}$) are used as the hole and electron sacrificial agents, respectively. The photocatalytic performance significantly decreases upon the addition of MeOH as the activation of benzyl alcohol with the hole is now prohibited. Adding $S_2O_8^{2-}$ should block O_2 from being reduced; however, we find that the performance metrics increase with the amount of $S_2O_8^{2-}$ added. This behavior arises from the fact that the direct oxidation processes are boosted by electron scavengers. It also proves that the holes generated with 365 nm LED irradiation are highly active for alcohol activation and oxidation. In order to evaluate the role of O_2 during the photocatalysis process, reactions under Ar are launched. The removal of O_2 is achieved with an argon (Ar) Schlenk line, and the CTB under this environment performs poorly due to the reduction and decomposition of Te^{4+} by the photogenerated electrons (**Figure S12**). The Ar experiments confirm that the photogenerated electrons are taken by O_2 in the case of aerobic oxidation conditions. Similar control experiments are applied for photocatalytic tests under 455 nm LED irradiation, and these control experiments reveal that even when the system is injected with large amounts of electron scavengers, the photogenerated holes excited by 455 nm light still yield very limited photocatalytic performances.

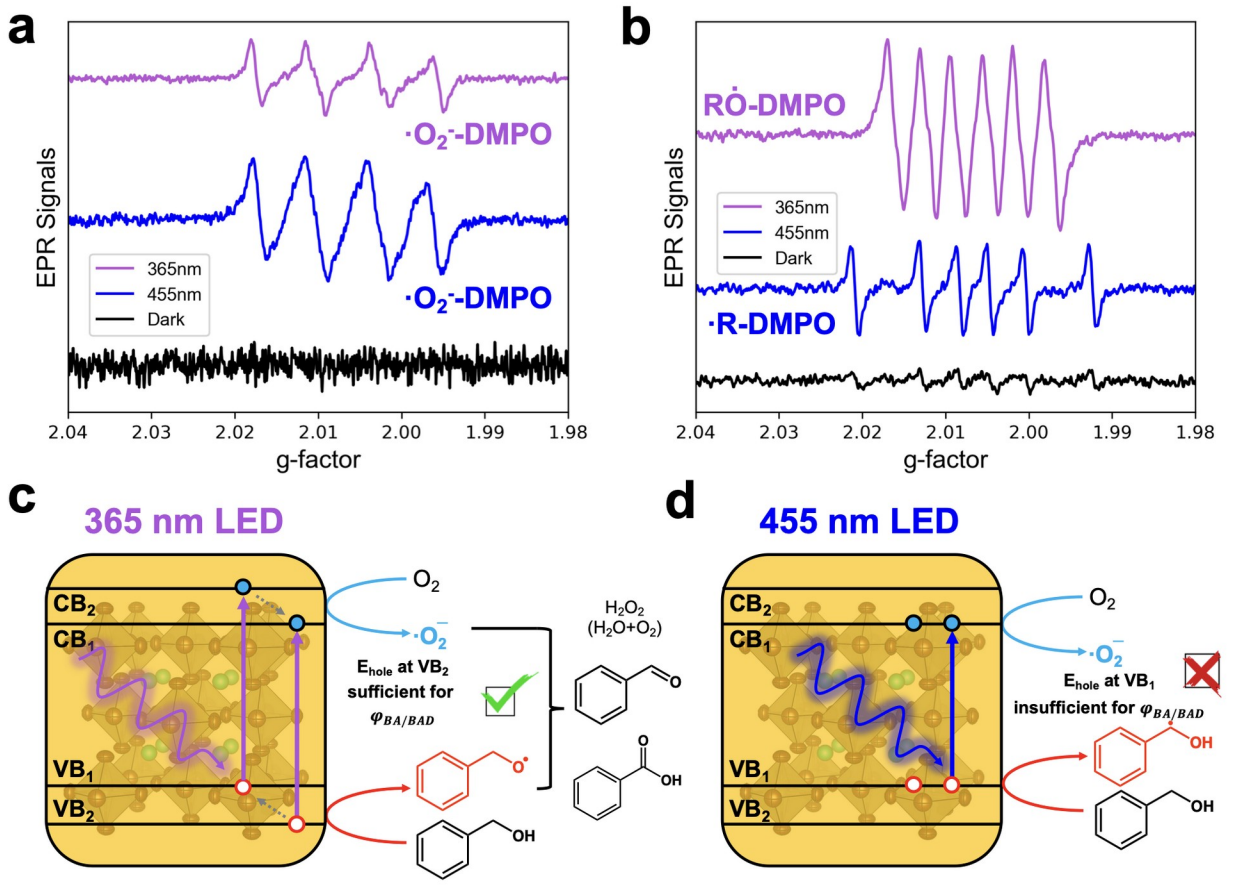

Figure 4. Reaction Mechanisms under 365 nm and 455 nm LED Irradiation. (a) EPR spectra for active oxygen radicals during the photocatalysis of Cs_2TeBr_6. Superoxide radical signals are detected under both excitation wavelengths. The broadening of EPR peaks under 365 nm excitation corresponds to the ring opening decomposition of the DMPO-·O_2^- species. (b) EPR spectra for active alcohol radicals during the photocatalysis of Cs_2TeBr_6 without O_2. The spectrum of the oxygen-centered alcohol radical is observed under the 365 nm LED, and a featured splitting corresponding to carbon-centered alcohol radical is observed under the 455 nm LED. (c, d) Schematics of the proposed photocatalytic benzyl alcohol oxidation reaction pathways under the two different light irradiations.

Electron paramagnetic resonance (EPR) spectroscopy with 5,5-Dimethyl-1-Pyrroline-N-Oxide (DMPO) is applied to measure the active reaction radical intermediates during the reactions. First, the superoxide radicals are observed under both excitation wavelengths (**Figure 4a**), which means that the photogenerated electrons under both wavelengths are sufficient for superoxide radical formation, in agreement with the CBM determined in **Figure 2**. The broadening of EPR peaks under 365 nm excitation corresponds to the ring opening

decomposition of the DMPO-·O_2^- species.[19] On the other hand, activated alcohol radicals are detected in the Ar atmosphere. Intriguingly, signals representing different types of alcohol radicals are observed under the two different light excitations (**Figure 4b**). The oxygen-centered alcohol radicals (·OR, alkoxy radicals) are detected under 365 nm LED irradiation, while the carbon-centered alcohol radicals (·R, alkyl radicals) are observed under 455 nm LED irradiation. This observation reveals that there are two different hole populations triggering the reactions under the different excitation wavelength, and the alcohols are activated in different molecular pathways. **Figure 4c** and **Figure 4d** summarize the reaction schematics for photocatalytic reactions under 365 nm LED and 455 nm LED. For 365 nm excitation, electrons from a deeper state, VB_2, can be excited to CB_1, with electronic transitions from VB_1 to CB_2 also occurring. The electrons in both CB_1 and CB_2 can be used to reduce the oxygen into superoxide radicals, while the energy-efficient holes generated in VB_2 can effectively form alkoxy radicals and carry out reactions toward BAD formation. The thermalizations of high energy electrons and holes may happen with a minor population suggested by the selection rule because of the same symmetry between HOMO (a_{1g}) and HOMO-1/-2 (a_{2g} and e_g), and between LUMO (a_{2u}) and LUMO+1 (e_u). When illuminated with a 455 nm LED, only the electrons in VB_1 are excited to CB_1 through the HOMO-to-LUMO transition. As a result, while the electrons in CB_1 is energy-efficient for producing superoxide radicals, the holes generated in VB_1 is energy-inefficient to BA oxidation. The formation of oxygen-centered or carbon-centered radicals is relevant to the adsorption and activation of the BA (**Figure S13**).[40] If the benzyl alcohols dissociate first, they will be activated into the alkoxy radicals. This reveals the fact that holes from the different VBs can create different activation pathways for benzyl alcohol. It opens the possibility to achieving

different reaction pathways or selectivity by controlling the wavelengths with which this molecule-like semiconductor photocatalyst is irradiated.

CONCLUSION

In summary, we have established the electronic band structure and photoexcitation pictures in the molecule-like halide perovskite Cs_2TeBr_6 based on the knowledge of the $[TeBr_6]^{2-}$ ionic octahedron. UV-vis absorption spectroscopy, VB-XPS, and LEIPS are used to obtain a comprehensive electronic band structure of this material. When applying this molecule-like halide perovskite for the photocatalytic aerobic oxidation of benzyl alcohol, we find that the 365 nm LED and 455 nm LED can generate holes in different valence bands and activate the benzyl alcohol molecules differently. EPR measurements clearly show the formation of oxygen-centered alcohol radicals under 365 nm LED and carbon-centered alcohol radicals under 455 nm LED. The photogenerated holes under 455 nm are energy insufficient; thus, only UV photons contribute to most of the photocatalytic performance. This study also establishes a new rational design principle for halide perovskites photocatalysts. With an understanding of $[MX_6]^{n-}$ octahedron molecular orbitals and energetic transitions, we can derive the electronic structures of halide perovskites, and we can apply a suitable light irradiation to drive certain photocatalytic reactions. The highly tunable energy band structures and catalytic centers in perovskites can offer a valuable platform for photocatalytic mechanistic studies and catalyst development in the foreseeable future.

ASSOCIATED CONTENT

Supporting Information

The Supporting Information is available free of charge on the ACS Publications website at DOI: Description of experimental details and additional characterization data. Figures showing SEM and EDS results, XPS spectra, and tables showing photocatalytic results, including Figures S1-S13, Tables S1-S6. (PDF)

AUTHOR INFORMATION

Corresponding Author

*Email: p_yang@berkeley.edu

ORCID

Jianbo Jin: 0000-0002-9054-7960

Haowei Huang: 0000-0002-2901-8189

Chubai Chen: 0000-0003-2513-2707

Maria C. Folgueras: 0000-0001-6502-7616

Sunmoon Yu: 0000-0001-7250-9365

Peng-Cheng Chen: 0000-0002-0411-9549

Peidong Yang: 0000-0003-4799-1684

Funding Sources:

This work was financially supported by the BASF CARA program (No. 047010). J.J., C.C., and Y.Z. acknowledge the fellowship support from Suzhou Industrial Park. H.H. acknowledges financial support from the Research Foundation – Flanders (1242922N and V407022N). M.C.F.

acknowledges support from the Kavli ENSI Philomathia Graduate Student Fellowship. S.Y. acknowledges support from Samsung Scholarship. VB-XPS measurements are carried out at the Molecular Foundry at Lawrence Berkeley National Lab (LBL). LEIPS was performed with help of Dr. Juliet Jamtgaard at the Stanford Nano Shared Facilities (SNSF), supported by the National Science Foundation (ECCS-2026822).

Notes:

The authors declare no competing financial interest.

ACKNOWLEDGEMENTS

J.J. thanks Mr. Zixi Zhu (The Scripps Research Institute) and Mr. Yehao Qiu (UC Berkeley) for their helpful discussions.

REFERENCES

(1) Manser, J. S.; Christians, J. A.; Kamat, P. v. Intriguing Optoelectronic Properties of Metal Halide Perovskites. *Chem. Rev.* **2016**, *116*, 12956–13008. https://doi.org/10.1021/acs.chemrev.6b00136.

(2) Kovalenko, M. v; Protesescu, L.; Bodnarchuk, M. I. Properties and Potential Optoelectronic Applications of Lead Halide Perovskite Nanocrystals. *Science* **2017**, *358*, 745. https://doi.org/10.1126/science.aam7093.

(3) Steele, J. A.; Lai, M.; Zhang, Y.; Lin, Z.; Hofkens, J.; Roeffaers, M. B. J.; Yang, P. Phase Transitions and Anion Exchange in All-Inorganic Halide Perovskites. *Acc. Mater. Res.* **2020**, *1*, 3–15. https://doi.org/10.1021/accountsmr.0c00009.

(4) Lee, M. M.; Teuscher, J.; Miyasaka, T.; Murakami, T. N.; Snaith, H. J. Efficient Hybrid Solar Cells Based on Meso-Superstructured Organometal Halide Perovskites. *Science* **2012**, *338*, 643. https://doi.org/10.1126/science.1228604.

(5) Burschka, J.; Pellet, N.; Moon, S.-J.; Humphry-Baker, R.; Gao, P.; Nazeeruddin, M. K.; Grätzel, M. Sequential Deposition as a Route to High-Performance Perovskite-Sensitized Solar Cells. *Nature* **2013**, *499*, 316–319. https://doi.org/10.1038/nature12340.

(6) Green, M. A.; Ho-Baillie, A.; Snaith, H. J. The Emergence of Perovskite Solar Cells. *Nat. Photonics* **2014**, *8*, 506–514. https://doi.org/10.1038/nphoton.2014.134.

(7) Snaith, H. J. Perovskites: The Emergence of a New Era for Low-Cost, High-Efficiency Solar Cells. *J. Phys. Chem. Lett.* **2013**, *4*, 3623–3630. https://doi.org/10.1021/jz4020162.

(8) Tan, Z.-K.; Moghaddam, R. S.; Lai, M. L.; Docampo, P.; Higler, R.; Deschler, F.; Price, M.; Sadhanala, A.; Pazos, L. M.; Credgington, D.; Hanusch, F.; Bein, T.; Snaith, H. J.; Friend, R. H. Bright Light-Emitting Diodes Based on Organometal Halide Perovskite. *Nat. Nanotechnol.* **2014**, *9*, 687–692. https://doi.org/10.1038/nnano.2014.149.

(9) Liu, X.-K.; Xu, W.; Bai, S.; Jin, Y.; Wang, J.; Friend, R. H.; Gao, F. Metal Halide Perovskites for Light-Emitting Diodes. *Nat. Mater.* **2021**, *20*, 10–21. https://doi.org/10.1038/s41563-020-0784-7.

(10) Ahmadi, M.; Wu, T.; Hu, B. A Review on Organic–Inorganic Halide Perovskite Photodetectors: Device Engineering and Fundamental Physics. *Adv. Mater.* **2017**, *29*, 1605242. https://doi.org/10.1002/adma.201605242.

(11) Chen, Q.; Wu, J.; Ou, X.; Huang, B.; Almutlaq, J.; Zhumekenov, A. A.; Guan, X.; Han, S.; Liang, L.; Yi, Z.; Li, J.; Xie, X.; Wang, Y.; Li, Y.; Fan, D.; Teh, D. B. L.; All, A. H.; Mohammed, O. F.; Bakr, O. M.; Wu, T.; Bettinelli, M.; Yang, H.; Huang, W.; Liu, X. All-Inorganic Perovskite Nanocrystal Scintillators. *Nature* **2018**, *561*, 88–93. https://doi.org/10.1038/s41586-018-0451-1.

(12) Yin, W.-J.; Shi, T.; Yan, Y. Unique Properties of Halide Perovskites as Possible Origins of the Superior Solar Cell Performance. *Adv. Mater.* **2014**, *26*, 4653–4658. https://doi.org/10.1002/adma.201306281.

(13) Gao, M.; Zhang, Y.; Lin, Z.; Jin, J.; Folgueras, M. C.; Yang, P. The Making of a Reconfigurable Semiconductor with a Soft Ionic Lattice. *Matter* **2021**, *4*, 3874–3896. https://doi.org/10.1016/j.matt.2021.09.023.

(14) Park, S.; Chang, W. J.; Lee, C. W.; Park, S.; Ahn, H.-Y.; Nam, K. T. Photocatalytic Hydrogen Generation from Hydriodic Acid Using Methylammonium Lead Iodide in Dynamic Equilibrium with Aqueous Solution. *Nat. Energy* **2016**, *2*, 16185. https://doi.org/10.1038/nenergy.2016.185.

(15) Wu, Y.; Wang, P.; Zhu, X.; Zhang, Q.; Wang, Z.; Liu, Y.; Zou, G.; Dai, Y.; Whangbo, M.-H.; Huang, B. Composite of $CH_3NH_3PbI_3$ with Reduced Graphene Oxide as a Highly Efficient and Stable Visible-Light Photocatalyst for Hydrogen Evolution in Aqueous HI Solution. *Adv. Mater.* **2018**, *30*, 1704342. https://doi.org/10.1002/adma.201704342.

(16) Singh, S.; Chen, H.; Shahrokhi, S.; Wang, L. P.; Lin, C.-H.; Hu, L.; Guan, X.; Tricoli, A.; Xu, Z. J.; Wu, T. Hybrid Organic–Inorganic Materials and Composites for Photoelectrochemical Water Splitting. *ACS Energy Lett.* **2020**, *5*, 1487–1497. https://doi.org/10.1021/acsenergylett.0c00327.

(17) Wang, X.-D.; Huang, Y.-H.; Liao, J.-F.; Jiang, Y.; Zhou, L.; Zhang, X.-Y.; Chen, H.-Y.; Kuang, D.-B. In Situ Construction of a Cs_2SnI_6 Perovskite Nanocrystal/SnS_2 Nanosheet Heterojunction with Boosted Interfacial Charge Transfer. *J. Am. Chem. Soc.* **2019**, *141*, 13434–13441. https://doi.org/10.1021/jacs.9b04482.

(18) Bhosale, S. S.; Kharade, A. K.; Jokar, E.; Fathi, A.; Chang, S.; Diau, E. W.-G. Mechanism of Photocatalytic CO_2 Reduction by Bismuth-Based Perovskite Nanocrystals at the Gas–Solid Interface. *J. Am. Chem. Soc.* **2019**, *141*, 20434–20442. https://doi.org/10.1021/jacs.9b11089.

(19) Huang, H.; Yuan, H.; Janssen, K. P. F.; Solís-Fernández, G.; Wang, Y.; Tan, C. Y. X.; Jonckheere, D.; Debroye, E.; Long, J.; Hendrix, J.; Hofkens, J.; Steele, J. A.; Roeffaers, M. B. J. Efficient and Selective Photocatalytic Oxidation of Benzylic Alcohols with Hybrid Organic–Inorganic Perovskite Materials. *ACS Energy Lett.* **2018**, *3*, 755–759. https://doi.org/10.1021/acsenergylett.8b00131.

(20) Zhu, X.; Lin, Y.; Sun, Y.; Beard, M. C.; Yan, Y. Lead-Halide Perovskites for Photocatalytic α-Alkylation of Aldehydes. *J. Am. Chem. Soc.* **2019**, *141*, 733–738. https://doi.org/10.1021/jacs.8b08720.

(21) Chen, K.; Deng, X.; Dodekatos, G.; Tüysüz, H. Photocatalytic Polymerization of 3,4-Ethylenedioxythiophene over Cesium Lead Iodide Perovskite Quantum Dots. *J. Am. Chem. Soc.* **2017**, *139*, 12267–12273. https://doi.org/10.1021/jacs.7b06413.

(22) Zhu, X.; Lin, Y.; San Martin, J.; Sun, Y.; Zhu, D.; Yan, Y. Lead Halide Perovskites for Photocatalytic Organic Synthesis. *Nat. Commun.* **2019**, *10*, 2843. https://doi.org/10.1038/s41467-019-10634-x.

(23) Dai, Y.; Poidevin, C.; Ochoa-Hernández, C.; Auer, A. A.; Tüysüz, H. A Supported Bismuth Halide Perovskite Photocatalyst for Selective Aliphatic and Aromatic C–H Bond Activation. *Angew. Chem. Intl. Ed.* **2020**, *59*, 5788–5796. https://doi.org/10.1002/anie.201915034.

(24) Huang, H.; Pradhan, B.; Hofkens, J.; Roeffaers, M. B. J.; Steele, J. A. Solar-Driven Metal Halide Perovskite Photocatalysis: Design, Stability, and Performance. *ACS Energy Lett.* **2020**, *5*, 1107–1123. https://doi.org/10.1021/acsenergylett.0c00058.

(25) Huang, H.; Verhaeghe, D.; Weng, B.; Ghosh, B.; Zhang, H.; Hofkens, J.; Steele, J. A.; Roeffaers, M. B. J. Metal Halide Perovskite Based Heterojunction Photocatalysts. *Angew. Chem. Intl. Ed.* **2022**, *61*, e202203261. https://doi.org/10.1002/anie.202203261.

(26) Xiao, Z.; Song, Z.; Yan, Y. From Lead Halide Perovskites to Lead-Free Metal Halide Perovskites and Perovskite Derivatives. *Adv. Mater.* **2019**, *31*, 1803792. https://doi.org/10.1002/adma.201803792.

(27) Maughan, A. E.; Ganose, A. M.; Scanlon, D. O.; Neilson, J. R. Perspectives and Design Principles of Vacancy-Ordered Double Perovskite Halide Semiconductors. *Chem. Mater.* **2019**, *31*, 1184–1195. https://doi.org/10.1021/acs.chemmater.8b05036.

(28) Folgueras, M. C.; Jin, J.; Gao, M.; Quan, L. N.; Steele, J. A.; Srivastava, S.; Ross, M. B.; Zhang, R.; Seeler, F.; Schierle-Arndt, K.; Asta, M.; Yang, P. Lattice Dynamics and Optoelectronic Properties of Vacancy-Ordered Double Perovskite Cs_2TeX_6 ($X = Cl^-, Br^-, I^-$) Single Crystals. *J. Phys. Chem. C* **2021**, *125*, 25126–25139. https://doi.org/10.1021/acs.jpcc.1c08332.

(29) Folgueras, M. C.; Louisia, S.; Jin, J.; Gao, M.; Du, A.; Fakra, S. C.; Zhang, R.; Seeler, F.; Schierle-Arndt, K.; Yang, P. Ligand-Free Processable Perovskite Semiconductor Ink. *Nano Lett.* **2021**, *21*, 8856–8862. https://doi.org/10.1021/acs.nanolett.1c03308.

(30) Shi, M.; Zhou, H.; Tian, W.; Yang, B.; Yang, S.; Han, K.; Li, R.; Li, C. Lead-Free B-Site Bimetallic Perovskite Photocatalyst for Efficient Benzylic C–H Bond Activation. *Cell Rep. Phys. Sci.* **2021**, *2*, 100656. https://doi.org/10.1016/j.xcrp.2021.100656.

(31) Dotsenko, A. A.; Shcheka, O. L.; Vovna, V. I.; Korochentsev, V. v; Mirochnik, A. G.; Sedakova, T. v. Electronic Structure and Luminescence of Tellurium (IV) Halide Complexes with Guanidine and Caesium Cations. *J. Mol. Struct.* **2016**, *1109*, 13–21. https://doi.org/10.1016/j.molstruc.2015.12.067.

(32) Dotsenko, A. A.; Vovna, V. I.; Korochentsev, V. v; Mirochnik, A. G.; Shcheka, O. L.; Sedakova, T. v; Sergienko, V. I. Halide Perovskite-Derived Compounds Rb_2TeX_6 (X = Cl, Br, and I): Electronic Structure of the Ground and First Excited States. *Inorg. Chem.* **2019**, *58*, 6796–6803. https://doi.org/10.1021/acs.inorgchem.9b00250.

(33) Couch, D. A.; Wilkins, C. J.; Rossman, G. R.; Gray, H. B. Electronic Energy Levels in Hexahalotellurate(IV) Complexes. *J. Am. Chem. Soc.* **1970**, *92*, 307–310. https://doi.org/10.1021/ja00705a014.

(34) Stufkens, D. J. Dynamic Jahn-Teller Effect in the Excited States of $SeCl_6^{2-}$, $SeBr_6^{2-}$, $TeCl_6^{2-}$ and $TeBr_6^{2-}$: Interpretation of Electronic Absorption and Raman Spectra. *Recueil des Travaux Chimiques des Pays-Bas* **1970**, *89*, 1185–1201. https://doi.org/10.1002/recl.19700891109.

(35) Sedakova, T. v; Mirochnik, A. G. Luminescent and Thermochromic Properties of Tellurium(IV) Halide Complexes with Cesium. *Opt. Spectrosc.* **2016**, *120*, 268–273. https://doi.org/10.1134/S0030400X16020223.

(36) Lugo, G.; Schwanen, V.; Fresch, B.; Remacle, F. Charge Redistribution Effects on the UV–Vis Spectra of Small Ligated Gold Clusters: A Computational Study. *J. Phys. Chem. C* **2015**, *119*, 10969–10980. https://doi.org/10.1021/jp511120j.

(37) Cheng, D.; Liu, R.; Hu, K. Gold Nanoclusters: Photophysical Properties and Photocatalytic Applications. *Front. Chem.* **2022**, *10*. https://doi.org/10.3389/fchem.2022.958626.

(38) Xiao, X.; Jiang, J.; Zhang, L. Selective Oxidation of Benzyl Alcohol into Benzaldehyde over Semiconductors under Visible Light: The Case of $Bi_{12}O_{17}Cl_2$ Nanobelts. *Appl Catal B* **2013**, *142–143*, 487–493. https://doi.org/10.1016/j.apcatb.2013.05.047.

(39) Nakata, K.; Fujishima, A. TiO_2 Photocatalysis: Design and Applications. *Journal of Photochemistry and Photobiology C: Photochemistry Reviews* **2012**, *13*, 169–189. https://doi.org/10.1016/j.jphotochemrev.2012.06.001.

(40) Shen, Z.; Hu, Y.; Li, B.; Zou, Y.; Li, S.; Wilma Busser, G.; Wang, X.; Zhao, G.; Muhler, M. State-of-the-Art Progress in the Selective Photo-Oxidation of Alcohols. *Journal of Energy Chemistry* **2021**, *62*, 338–350. https://doi.org/10.1016/j.jechem.2021.03.033.

(41) Qi, M.-Y.; Conte, M.; Anpo, M.; Tang, Z.-R.; Xu, Y.-J. Cooperative Coupling of Oxidative Organic Synthesis and Hydrogen Production over Semiconductor-Based Photocatalysts. *Chem. Rev.* **2021**, *121*, 13051–13085. https://doi.org/10.1021/acs.chemrev.1c00197.

For Table of Contents Use Only

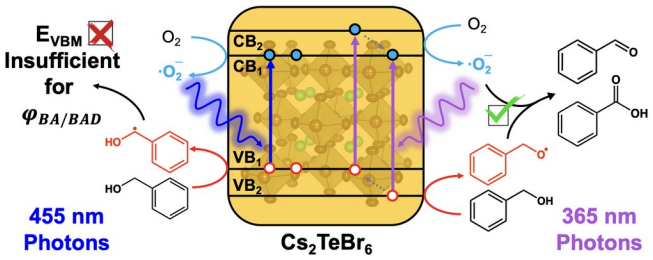

Title: Benzyl Alcohol Photo-oxidation based on Molecular Electronic Transitions in Metal Halide Perovskites

Authors: Jianbo Jin[#], Haowei Huang[#], Chubai Chen, Patrick W. Smith, Maria C. Folgueras, Sunmoon Yu, Ye Zhang, Peng-Cheng Chen, Fabian Seeler, Bernd Schaefer, Carlos Lizandara-Pueyo, Rui Zhang, Kerstin Schierle-Arndt, and Peidong Yang[*]

Synopsis: The molecular electronic structure of zero-dimensional (0D) halide perovskites, Cs_2TeBr_6, enables distinct electronic transitions, which can be applied to efficient photocatalytic reactions.